

Numerical simulation of confined flows past obstacles – the comparative study of Lattice Boltzmann and Spectral Element Methods

W. REGULSKI, J. SZUMBARSKI

*Faculty of Power and Aeronautical Engineering
Institute of Aeronautics and Applied Mechanics
Warsaw University of Technology
Nowowiejska 24
00-665 Warszawa, Poland
e-mails: wregulski@meil.pw.edu.pl, jasz@meil.pw.edu.pl*

THIS PAPER CONCERNS THE LATTICE BOLTZMANN METHOD (LBM) which has recently become alternative, computationally efficient tool to simulate a Newtonian fluid flow, especially in complex geometries. A series of benchmark two-dimensional simulations with the LBM are presented and analyzed in order to assess the impact of the LBM grid refinement on the results of the simulations. The considered cases include stationary and time-dependent flows past a circular or a 45-degree rotated square cylinder confined in the channel with parallel walls. Next, the same flow configurations are investigated by means of the Spectral Element Method (SEM) and obtained results are used to cross-validate both approaches. The sensitivity to the resolution of representation of the obstacle's shape in the LBM simulations is of the main interest. Particular attention is paid also to the effects of compressibility of the flow. Additionally, for unsteady flows the transient flow characteristics are compared in detail: the velocity profiles from the LBM and SEM are presented and some non-dimensional characteristics such as Strouhal number of the compared von Karman vortex streets.

Key words: Lattice Boltzmann Method, Spectral Element Method, flow past cylinder.

Copyright © 2012 by IPPT PAN

1. Introduction

THE LATTICE BOLTZMANN METHOD is a relatively new approach to simulate fluid flows. It is based on the kinetic approach to fluid motion and originates from the Boltzmann Transport Equation from the classical kinetic theory of gases. The LBM appeared as a spin-off of the Lattice Gas Cellular Automata (LGCA) at the end of the 80s of the past century [1]. LGCA were a set of numerical techniques that aimed to reproduce the dynamics of multi-particle systems by creating a binary dynamical system with a certain set of collision rules of strictly local nature. The LBM became an independent field of research as soon as its remarkable po-

tential to simulate various kinds of physical phenomena was realized. Nowadays, although still in rapid development stage, LBM is a well-established alternative when it comes to simulating various types of fluid flows including turbulence [2], magnetohydrodynamics [3], multicomponent flows across complicated geometries [4] to multiphase flows with phase change [5]. Main advantage of the LBM over the classical approach to solving Navier Stokes equations is its remarkable conceptual simplicity, ease of implementation, predestination to massively parallel computing [6] and straightforward implementation of geometry.

In this paper, the simplest form of the LBM, namely LBM with Bhatnagar–Gross–Krook (BGK) collision operator, is presented for simulation of Newtonian fluid flows. The main part is focused around the flow of an incompressible Newtonian fluid past a circular or square cylinder in a confined geometry. Square cylinder obstacle is rotated by 45° from horizontal direction and is referred as “diamond”. Mathematically, the aim of the simulation is to find the solution of the governing equations:

$$(1.1) \quad \partial_t \mathbf{u} + (\mathbf{u} \cdot \nabla) \mathbf{u} = -\nabla p + \nu \Delta \mathbf{u},$$

$$(1.2) \quad \nabla \cdot \mathbf{u} = 0,$$

in the domain Ω depicted in Fig. 1. The boundary $\partial\Omega$ of the flow domain consists of three parts: the material part Γ_1 , which is the sidewall of the channel, the material part Γ_2 , which is the sidewall of the obstacle and the inlet and outlet sections denoted respectively as S_{in} and S_{out} . The sidewalls of the channel and the obstacle are impermeable and motionless, hence the boundary condition enforced at Γ_1 and Γ_2 is $\mathbf{u}|_{\Gamma} = \mathbf{0}$.

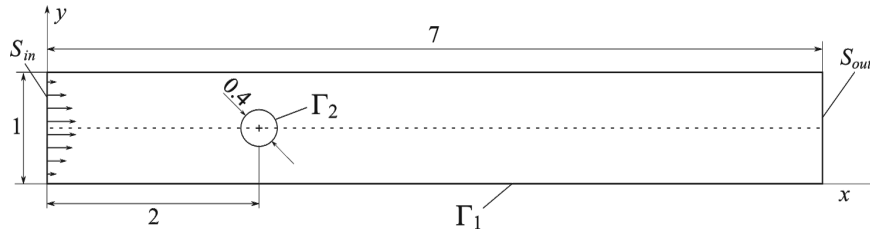


FIG. 1. The wall-confined flow past a circular cylinder – dimensions and boundary of the computational domain.

The aim of the paper is to validate the LBM with use of the Spectral Element Method in the regime of low and moderate Reynolds numbers (10 to 200), i.e., in both steady and unsteady flow regimes. The first regime is inspected in terms of the average pressure drop while the latter in terms of average quantities such as pressure drop as well as the Strouhal number of the von Karman vortex street that appears behind the obstacle.

The flows in confined geometries serve as a typical benchmark for any numerical method and were performed also with use of the LBM immediately after the invention of the method [7] and appeared later in [8]. They were also validated with use of the Finite Volume Method [9], but only the flow past a square obstacle parallel to the channel walls was investigated. Confined flows past rectangular and circular geometries have also been studied extensively by means of other methods [10, 11], where various issues like an effect of the blockage ratio $BR = D/H$ (D – diameter of the obstacle, H – channel height) or the inlet velocity profile on the critical Reynolds and/or Strouhal numbers of the vortex wake were investigated. This paper, however, deals only with a fixed blockage ratio and varying values of Reynolds number. The literature is really rich when it comes to investigation of flows past circular obstacles and also considerable number of papers dealing with a flow past a square can be found. However, the data concerning the wall-confined flows past diamond-shaped bodies is rare [12].

The paper is organized as follows: Section 2 presents the Lattice Boltzmann Method, its derivation, basic boundary conditions and typical issues necessary to set up an LBM simulation. Section 3 is devoted solely to simulations performed with LBM. Section 4 presents the Spectral Element Method. The simulations of flow past an obstacle performed with LBM and SEM are discussed and compared in Sec. 5. The results of the paper are briefly summarized in Sec. 6.

2. The Lattice Boltzmann Method

2.1. Method overview

Conventional approaches to simulate fluid flows rely on various discretizations of the Navier–Stokes equation which describes the motion of fluid treated as continuum. In contrast, the Lattice Boltzmann Method (LBM) originates from the Boltzmann transport equation, a fundamental equation in the kinetic theory of gases that describes the motion and interaction of particle populations in the phase space. This equation has the standard form

$$(2.1) \quad \frac{\partial f}{\partial t} + \mathbf{v} \cdot \nabla_{\mathbf{x}} f + \frac{\mathbf{F}}{m} \cdot \nabla_{\mathbf{v}} f = \iint \sigma(\Omega) |\mathbf{v} - \mathbf{v}_1| \cdot [f(\mathbf{v}') \cdot f(\mathbf{v}'_1) - f(\mathbf{v}) \cdot f(\mathbf{v}_1)] d\Omega d\mathbf{v}_1,$$

where $f = f(t, \mathbf{x}, \mathbf{v})$ stands for the probability density function (PDF) of finding a particle in the position \mathbf{x} with velocity \mathbf{v} in the phase space and \mathbf{F} denotes the external force field acting on the molecules of mass m . The left hand side of the equation represents the advection of the PDF in the phase space whereas the right hand side, the Boltzmann collision integral, is the balance of the PDF due

to molecular collisions. There, primed velocities ($\mathbf{v}', \mathbf{v}'_1$) represent the admissible post-collision velocities, σ denotes the differential collision cross-section and the total balance is obtained after integration of PDF of collisions over whole solid angle Ω and all velocities \mathbf{v}_1 .

The LBM is based on the so-called Lattice Boltzmann Equation that can be interpreted as a discretized form of the Boltzmann Transport Equation. The discretization procedure consists of a few steps. First, the equation is discretized in space and time. The space discretization takes place on the Cartesian grid. Additionally, the velocity space is limited to a finite number of velocities \mathbf{c}_i , $i = 0, 1, 2, \dots, M$. The convention used in the LBM is to denote different distribution functions at certain location \mathbf{x}_k with different subscripts: $f(t, \mathbf{x}_k, \mathbf{c}_i) \rightarrow f_i(t, \mathbf{x}_k)$, $i = 0, 1, 2, \dots, M$. The admissible velocities are those which let particles move exactly to neighboring nodes in one time step. In two dimensions, velocity space is usually limited to nine directions and in three dimensions one usually uses 15, 19 or 27 vectors (see Fig. 2). Other grids, however, are also admissible, e.g., the hexagonal grid in 2D. In general, the set of velocities is admissible if it has sufficient symmetries to ensure conservation of mass, momentum and momentum flux [13].

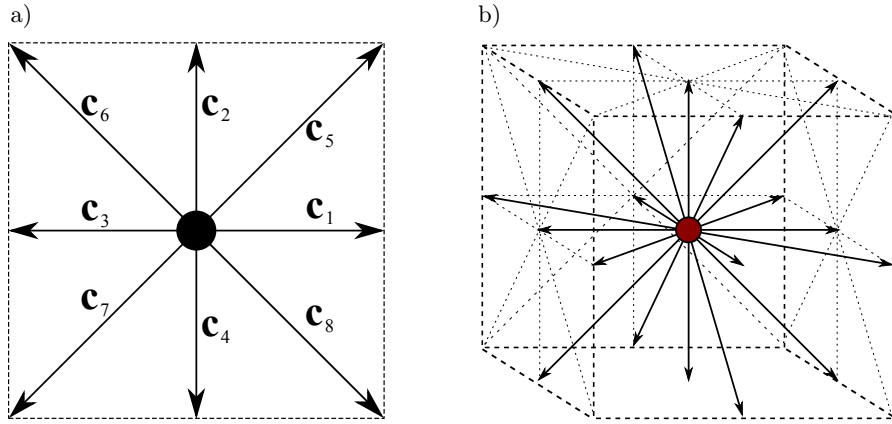


FIG. 2. a) D2Q9 lattice, b) D3Q19 lattice.

The Lattice Boltzmann Equation (LBE), the core of whole LBM states the relation between the particle population in one time step located in a certain node \mathbf{x} and population in the next time step that neighbors the node from the direction in which the population moves ($\mathbf{x} + \mathbf{c}_i \Delta t$). It takes the following form:

$$(2.2) \quad f_i(\mathbf{x} + \mathbf{c}_i \Delta t, t + \Delta t) - f_i(\mathbf{x}, t) = \Omega(f),$$

with Ω as the collision operator. The LBE can be viewed as two-stage process: first, all PDFs are transferred to neighboring locations (the streaming process,

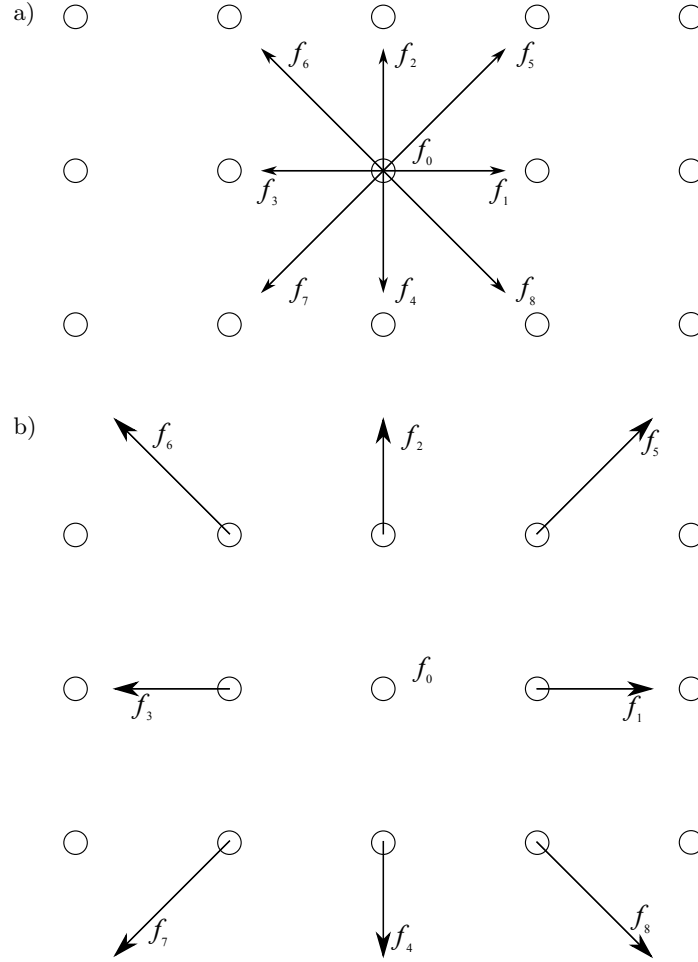


FIG. 3. Conceptual view of streaming process on D2Q9 lattice: each PDF is transferred to the neighboring lattice node.

Eq. (2.3) and Fig. 3). Then PDFs' values are updated because of molecular collisions:

$$(2.3) \quad f_i^{\text{pre-collision}}(\mathbf{x} + \mathbf{c}_i \Delta t, t + \Delta t) = f_i(\mathbf{x}, t),$$

$$(2.4) \quad f_i^{\text{post-collision}}(\mathbf{x} + \mathbf{c}_i \Delta t, t + \Delta t) = f_i^{\text{pre-collision}}(\mathbf{x} + \mathbf{c}_i \Delta t, t + \Delta t) + \Omega(f).$$

Regarding collision operators, any operator that preserves mass, momentum and momentum flux can be used in the LBE. The operator used in this work is known as single-relaxation-time BGK collision operator. The abbreviation BGK originates from the names of three authors (Bhatnagar, Gross and Krook,

see [16]). There exist more sophisticated models such as, e.g., multiple-relaxation-time [14, 17] that improve the stability of the algorithm for high Reynolds number flows. In this work, however, the BGK turned out to be sufficient. The LBE with BGK collision operator takes particularly simple form:

$$(2.5) \quad f_i(\mathbf{x} + \mathbf{c}_i \Delta t, t + \Delta t) - f_i(\mathbf{x}, t) = \frac{1}{\tau} (f_i^{\text{eq}} - f_i), \quad i = 0, 1, 2, \dots, M.$$

The coefficient of proportionality τ is the collision relaxation time which is related to the sheer viscosity of fluid by the formula:

$$(2.6) \quad \nu = c^2 \left(\tau - \frac{\Delta t}{2} \right),$$

where c denotes the lattice speed of sound, $c = 1/\sqrt{3}$ in this model. Relaxation time (and viscosity) is a tunable parameter in the simulation and has influence on the stability and accuracy of the method [14, 15]. Time step is usually set to unity $\Delta t = 1$.

In the BGK model, the new population is updated by the amount of particles proportional to the deviation of the population's state from the local equilibrium expressed by f_i^{eq} , which is the linearized form of the Maxwell–Boltzmann equilibrium distribution:

$$(2.7) \quad f_i^{\text{eq}} = w_i \rho \left[1 + \frac{\mathbf{c}_i \cdot \mathbf{u}}{c^2} + \frac{(\mathbf{c}_i \cdot \mathbf{u})^2}{2c^4} - \frac{\mathbf{u}^2}{2c^2} \right],$$

where \mathbf{u} is the local resultant velocity vector, $w_0 = 4/9$, $w_{i=1,\dots,4} = 1/9$, $w_{i=5,\dots,9} = 1/36$ are weight coefficients and ρ is the density of fluid in the node.

The LBE is solved in the non-dimensional form. Non-dimensionalization of the equations has been performed in a way that requires the density functions in one point to sum up to unity:

$$(2.8) \quad \sum_{i=0}^8 f_i = 1.$$

Macroscopic velocity and actual density of fluid (close to unity) are recovered with the following formulas:

$$(2.9) \quad \mathbf{u} = \frac{1}{\rho} \sum_{i=0}^8 c_i \cdot f_i,$$

$$(2.10) \quad \rho = \sum_{i=0}^8 f_i.$$

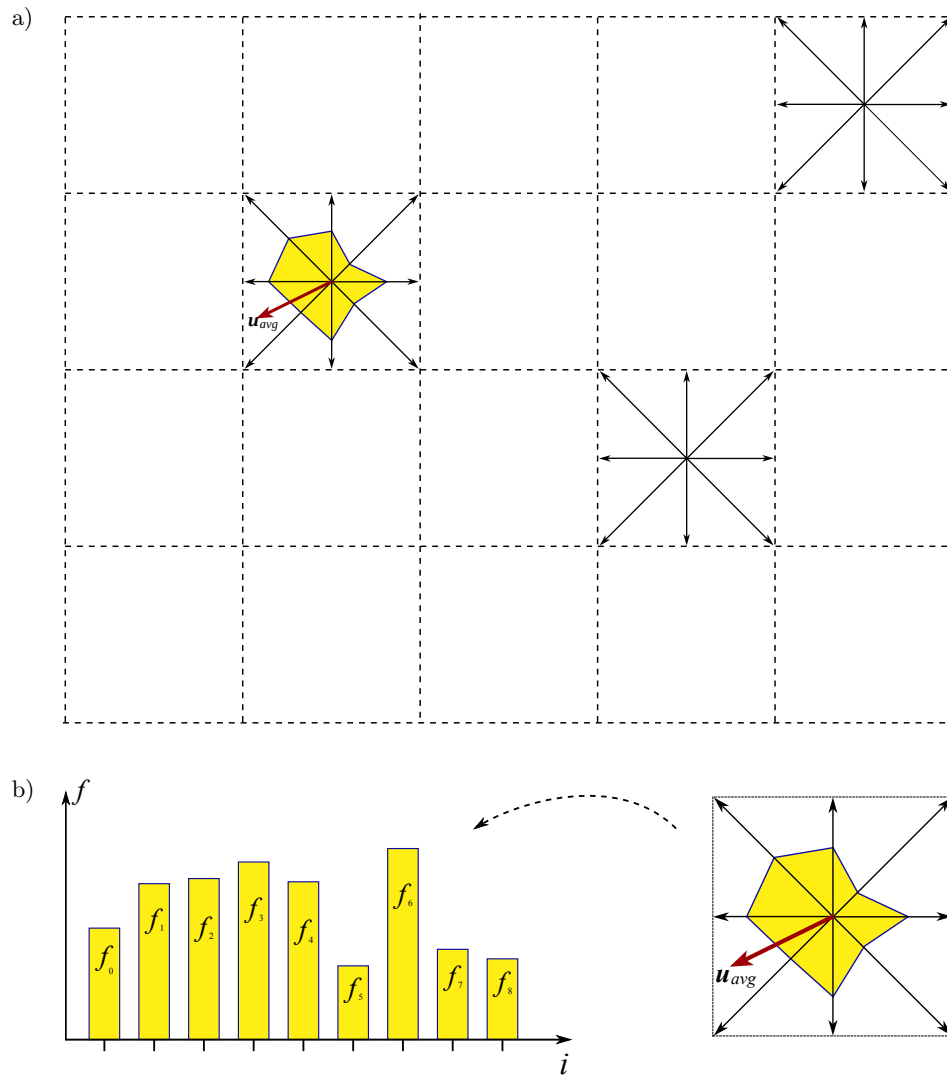


FIG. 4. a) The D2Q9 lattice with nine velocity directions. b) Density functions in appropriate directions and resultant macroscopic velocity.

The graphical interpretation of Eq. (2.9) is shown in Fig. 4. It should be noted that the LBM admits some variations of the fluid density, meaning that the fluid in this approach is inherently compressible and compressibility effects will inevitably occur during the simulation. Thus, the incompressibility constrain can be imposed only approximately, providing that the local Mach number of the lattice gas is sufficiently small. The pressure in the fluid is

connected with density by the relation

$$(2.11) \quad p = c^2 \rho.$$

Pressure variations can thus be directly recovered from density fluctuations. It is important to underline that the Lattice Boltzmann Equation reproduces the behavior of a Newtonian fluid only in the limit of the Mach number going to zero ($\text{Ma} \rightarrow 0$). In case of stronger compressibility effects, the results of the simulations should by no means be interpreted as simulations of compressible flow. In fact, the effects connected with the increased Mach number spoil the isotropy of the pressure tensor in the Navier–Stokes equation [21].

2.2. Boundary conditions

In contrast to “conventional” approaches in CFD, where generation of computational mesh is often a non-trivial task, the LBM enables straightforward implementation of geometries of arbitrary complexity (represented, however, by stair-case approximation). The no-slip condition on the material wall is realized by the so-called “bounce-back” rule. It forces the average local velocity at the wall to zero by reversing the directions on the PDFs approaching the wall, as shown in Fig. 5. The “bounce-back” boundary condition also imposes the form of the implementation of geometry to the LBM. It has to be provided in the form of a boolean mask, where zero elements will denote fluid nodes while non-zero elements will denote solid nodes.

Obviously, the “stair-case” form of geometry makes it impossible to appropriately reproduce shapes other than horizontal and vertical walls (see Fig. 6). The question of influence of such a surface roughness on the flow quality, especially on the pressure drop, arises. This issue is studied deeper in the further section of this paper. There exist methods to incorporate curvilinear geometry to the LBM simulations [23, 24]. In this work, however, the “bounce-back” method turns out to be sufficient and the effects of “stair-case” do not play any significant role. It should be stressed that the version of “bounce-back” boundary condition used here, namely the so-called “mid-wall” bounce back, gives second-order accuracy [15].

From multiple available kinds of open boundary conditions for the LBM [15, 18–20] the most common, yet very robust and simple are velocity and pressure boundary conditions [15]. They are demonstrated on the example of 2D channel flow with velocity inlet on the left and pressure outlet on the right (see Fig. 7). In general, these boundary conditions in the LBM link the PDFs leaving the computational domain with the ones that are injected into the domain.

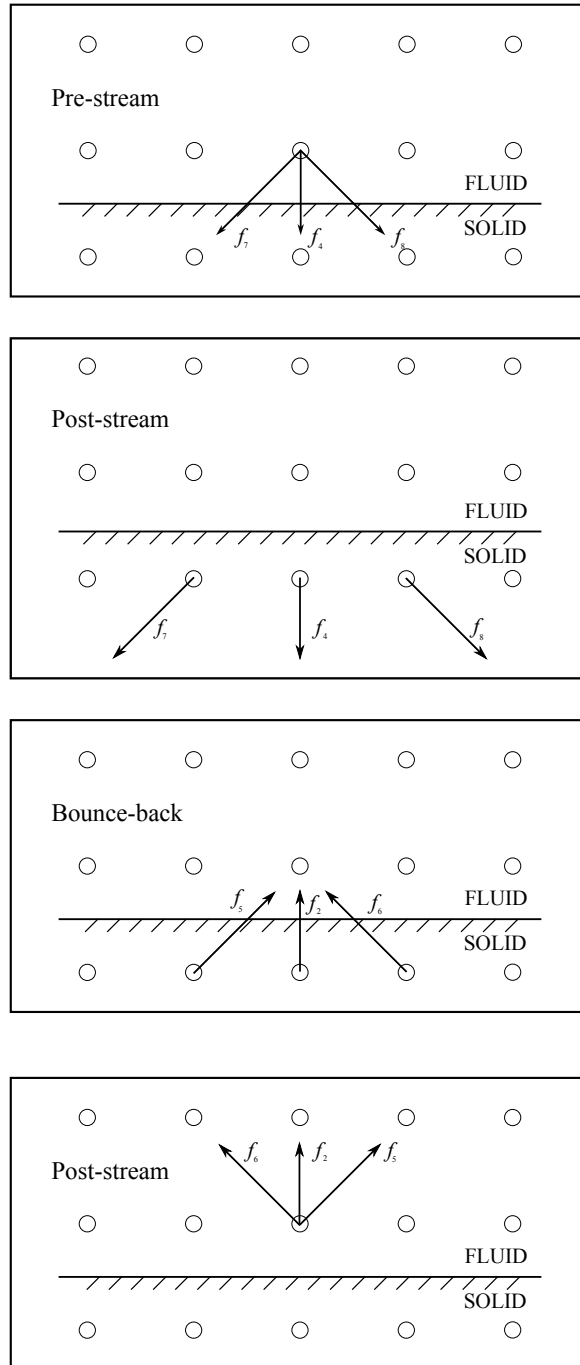


FIG. 5. The bounce-back rule. As a numerical artifact, a non-zero velocity inside the wall appears.

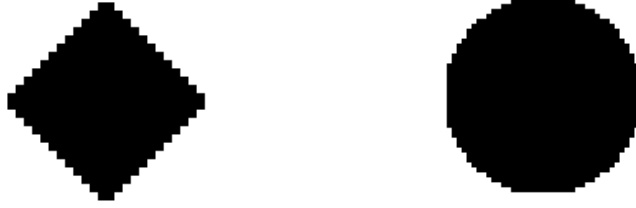


FIG. 6. The graphical implementation of the geometry to a 2-dimensional simulation. A diamond-shaped obstacle and a circle. Raster geometry clearly visible.

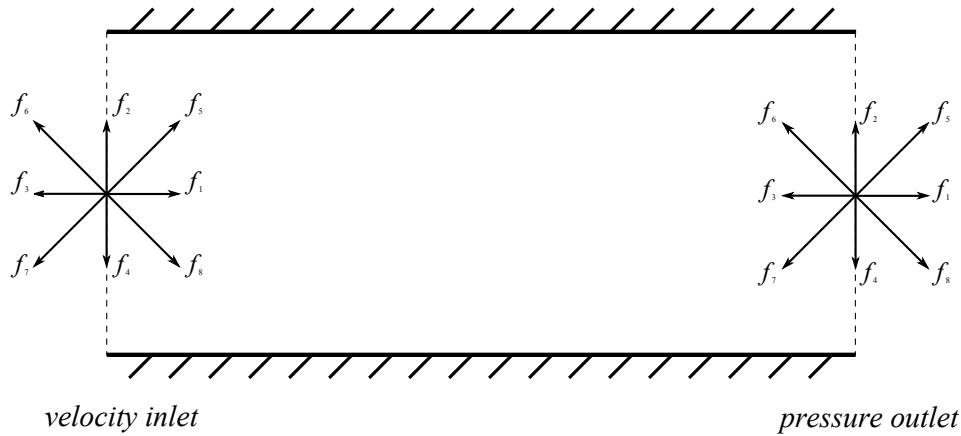


FIG. 7. Distribution functions at the inlet and at the outlet from the channel for a D2Q9 lattice [15].

2.3. Conversion of units in the Lattice Boltzmann Simulation

The recovery of physical values from the simulations performed with the LBM is based on the similitude of flows. The relevant similitude number is the Reynolds number which links the fluid velocity (U or U_{LB}), characteristic dimension D for the considered flow (or N , i.e., the number of the grid cells along this dimension) and the fluid kinematic viscosity (ν or ν_{LB})

$$(2.12) \quad \text{Re} = \frac{U \cdot D}{\nu} = \frac{U_{LB} \cdot N}{\nu_{LB}}.$$

The key question in the lattice Boltzmann simulation is the relation of the physical time step to the lattice time step. The reasoning goes as follows: the time (in seconds) needed to travel particular distance in the physical domain is

$$(2.13) \quad T = \frac{D}{U} \text{ [s]}.$$

In the non-dimensional domain the same time (in the lattice time unit ts) can be expressed as

$$(2.14) \quad T_{LB} = \frac{N}{U_{LB}} [ts].$$

Obviously, these times correspond to each other if

$$(2.15) \quad \frac{D}{U} = \frac{N}{U_{LB}}.$$

Lattice size N is expressed in the lattice length units [lu]. Taking into account the fact that the Reynolds numbers are the same and substituting for the velocity (which might be unknown before the simulation) one gets

$$(2.16) \quad \frac{D^2}{\nu} = \frac{N^2}{\nu_{LB}}.$$

That means that the actual time step in the LBM is expressed as

$$(2.17) \quad ts = \frac{D^2 \nu_{LB}}{N^2 \nu} [s].$$

This result also proves that the physical time step is resolution and viscosity-dependent. Thus, in order to achieve bigger time steps, one needs to decrease the resolution of the computational grid (and increase the lattice viscosity ν_{LB} to keep Re constant). This results, however, in the increased Mach number in the flow what puts a serious limitation on the increase of the time step. Additionally, the LBM is second-order accurate in time and space [25] so the time step and lattice resolution should be kept small compared to, e.g., Spectral Element Method used in this article.

2.4. Summary

The Lattice Boltzmann Method is conceptually a really simple tool to simulate the flow of a Newtonian fluid. The algorithm can be summarized in a few steps:

1. Streaming – motion of particles’ populations (represented by PDF) in time and space on the regular grid (see Fig. 3).
2. Collision – the interaction of particles’ populations during streaming with one another.
3. Bounce back – the interaction of particles with solid walls.

Advantages of the LBM concern efficient implementation of the algorithm and insensitivity to the complexity of geometry. Additionally, the algorithm is purely local, what predestines the LBM to massively parallel computations.

However, the method has a few important drawbacks. First of all, the Lattice Boltzmann Method reproduces the behavior of Newtonian fluid in the limit of no-compressibility [21]. That puts a very strong limitation on the method. In practice, in order to admit higher physical velocities the computational grid has to be refined. However, the values of flow variables are non-dimensionalized with respect to the lattice size. Thus, every change of the lattice resolution results in the change of the relation between the lattice and physical time steps or relation between lattice and physical velocities. Hence, setting up an LBM simulation is not so straightforward. Finally, the LBM memory requirements are much bigger than in the classical CFD solvers due to the fact that, apart from velocity and pressure/density value, all PDFs have to be stored.

The simulations for this paper were performed using the open-source code PALABOS [22]. The PALABOS is written in C++ and it is very well scalable on multi-core units. All simulations presented were performed on a cluster using up to 40 processors.

3. Analysis of accuracy of the Lattice Boltzmann Method

3.1. The study of roughness effects on the quality of simulations based on the LBM

An immediate issue which arises in the LBM is the impact of the raster form of the geometry on the quality of the flow simulation. In order to investigate this matter, a series of simulations of flows past an obstacle has been performed. The confined flows past a circular and revolved square-shaped (the so-called “diamond”) cylinders were simulated, see Fig. 8.

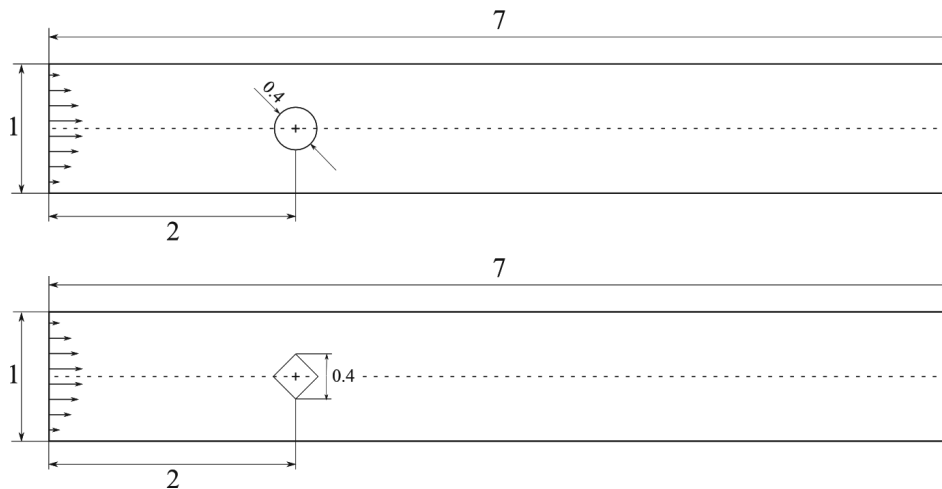


FIG. 8. Dimensions of the channel with immersed obstacles.

The channel was seven units long and the blockage ratio of the obstacle (the portion of the channel height obscured by the obstacle) was set to 0.4. The flow was forced at the inlet section with a parabolic velocity profile. The outlet boundary condition was set to constant pressure. The top and bottom walls were impermeable and motionless. The Reynolds number was equal to 40: it was based on the bulk velocity, obstacle diagonal or diameter and fluid viscosity:

$$(3.1) \quad \text{Re} = \frac{U_{\text{avg}} H}{\nu} = 40.$$

Since the simulation was performed in the non-dimensional units, an alternative expression for the Reynolds number based on the grid dimensions is valid:

$$(3.2) \quad \text{Re} = \frac{U_{\text{LB avg}} N_{\text{obst}}}{\nu_{\text{LB}}} = 40.$$

The flow at this value of Reynolds number is laminar and steady. Simulations were performed on the grids of different sizes ranging from 50 to 900 elements across the channel height. Obviously, the finer the grid, the more accurate is the representation of the obstacle. Figure 9 gives an idea about how a “diamond” and a “circle” are represented in the LBM.

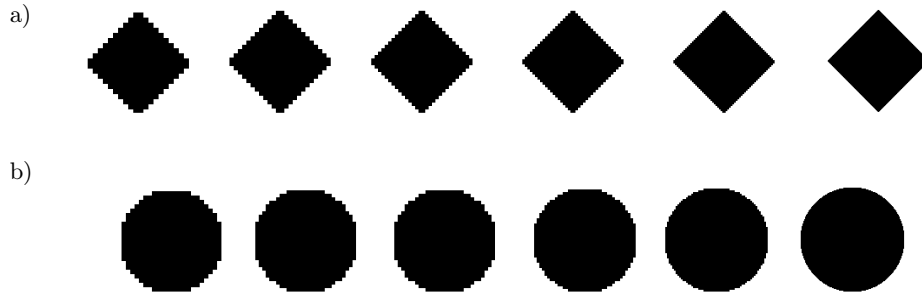


FIG. 9. The raster representation of the diamond and circular obstacle for the raster sizes ranging from 20 lu up to 120 lu.

The only criterion of the “smoothness” of the obstacle was the pressure drop along the channel. Each simulation was run with different viscosity so that the Mach number and lattice velocity were kept constant:

$$(3.3) \quad U_{\text{inlet max}} = 0.03 \left[\frac{\text{lu}}{\text{ts}} \right].$$

The simulation was initialized with a non-physical velocity field and the computations continued until the steady flow was obtained. The values of viscosity and obtained non-dimensional pressure drop for both cases are shown in Table 1.

Table 1. The parameters for simulations and the obtained pressure drops.

Simulation	N_{channel}	N_{obstacle}	ν_{LB}	Δp_{circle}	$\Delta p_{\text{diamond}}$
1	50	20	0.010	0.001027	0.001068
2	60	24	0.012	0.001015	0.001055
3	75	30	0.015	0.001018	0.001044
4	100	40	0.02	0.001014	0.001029
5	150	60	0.03	0.001010	0.001024
6	300	120	0.06	0.001006	0.001015
7	450	180	0.09	0.001006	0.001012
8	600	240	0.12	0.001005	0.001011
9	900	360	0.18	0.001004	0.001010

The pressure drops as a function of resolution of the grid are also presented in Fig. 10. Figure 11 shows the contour maps of the velocity magnitude in both flows.

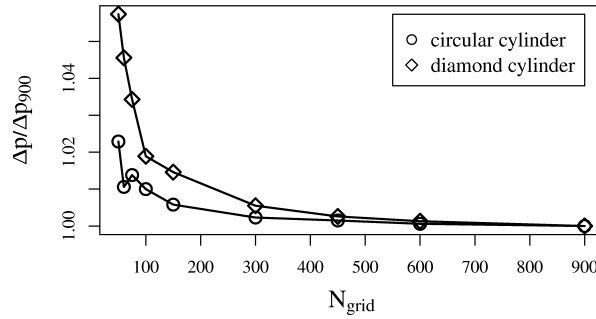


FIG. 10. The relative pressure drop in the flows past obstacles as a function of the resolution of the grid: the reference pressure for both cases is the pressure at maximum resolution denoted as Δp_{900} .

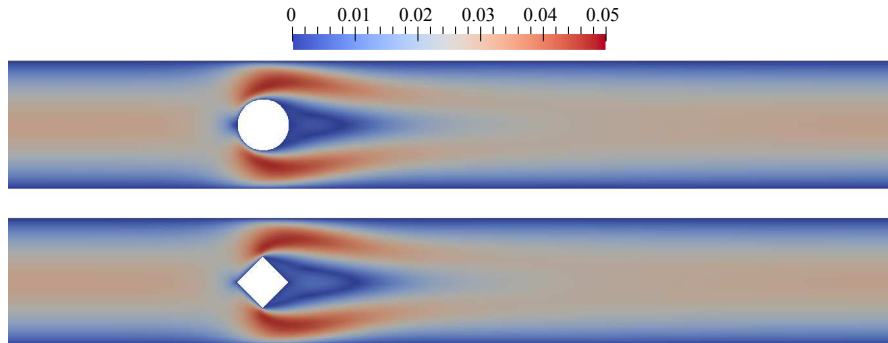


FIG. 11. Contour maps of the velocity magnitude of the steady symmetric flow past a confined diamond and circular obstacles at $\text{Re} = 40$. Lattice resolution: 600×4200 , $v_{\text{max diamond}} = 0.0471$, $v_{\text{max circle}} = 0.0473$.

The simulations show that the resistance to the flow drops with increasing resolution of the obstacle representation. The improvement is much more significant in the case of diamond-shaped obstacle. This can be attributed to the fact that the flow field around an obstacle with a sharp edge has (at least theoretically) arbitrarily large vorticity at the side corners. That cannot obviously be reproduced numerically (in none of the methods used in this study), but such a rapid change of direction in the flow spoils the simulation locally and has the effect on the overall result. In case of finer grids, this effect is more localized and thus the flow simulation is more accurate globally.

3.2. Flow past a diamond-shaped obstacle – the influence of the compressibility on the quality of the LBM simulation

Another test case for the Lattice Boltzmann Method was the simulation of flow past a diamond at Reynolds number $Re = 200$. At this value, the von Karman vortex street produced by the obstacle is very intensive and the interaction between the vortices and the channel walls is very strong. The dimensions of the channel were the same as before. The boundary conditions were the same as well: parabolic velocity inlet with constant pressure outlet. The simulations were, however, performed on huge grids, namely 300×2100 , 450×3150 and 600×4200 . This time, Mach numbers varied. The control values for the simulations are shown in Table 2.

Table 2. The control parameters for the flow past the diamond-shaped obstacle. The Mach number is based on the maximum inlet velocity.

Simulation	N_{channel}	U_{inlet}	ν_{LB}	Mach number (Ma)
1	200	0.075	0.02	0.129
2	300	0.050	0.02	0.086
3	300	0.025	0.01	0.043
4	450	0.033	0.02	0.053
5	600	0.025	0.02	0.043

The mass flow rate on the consecutive cross-sections, shown in Fig. 12, in two phases of vortex shedding was investigated. The vortex shedding is time-periodic and its phase is measured with respect to such instant when the vertical component of velocity probed at the control point (the center of the channel) changes its sign from negative to positive. This convention is applied in the whole paper.

It was found that the mass flow rate variations in the computational domain are most significant in case of the smallest resolution and biggest viscosity. They

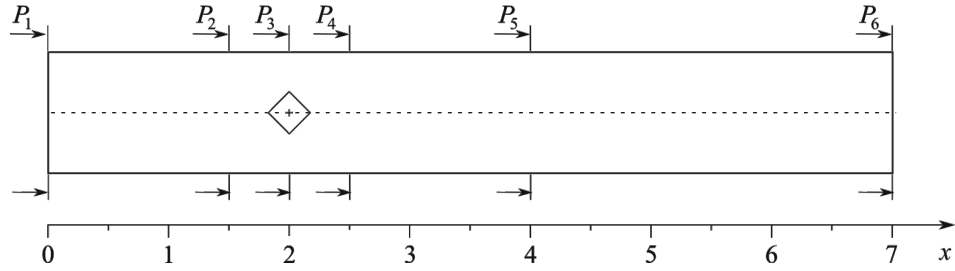


FIG. 12. The cross-sections at which velocity profiles and mass-flow rates were taken. The cross in the middle of the channel is the marker for probing the vertical velocity.

drop as the size of the grid increases (the Mach number drops). The mass flow rate variations were computed every quarter of the time period of the cyclic vortex shedding, with the time reference point as described above. Here, we present the results only for the phase '0' and the phase '1/4', i.e., a quarter of the time period after the beginning of the vortex shedding cycle. The flow patterns for the phase '1/2' and '3/4' are similar modulo mirror symmetry.

The relative mass flow rate on the consecutive cross-sections in the channel, normalized with respect to the inlet flow rate, is presented in the Fig. 13. It

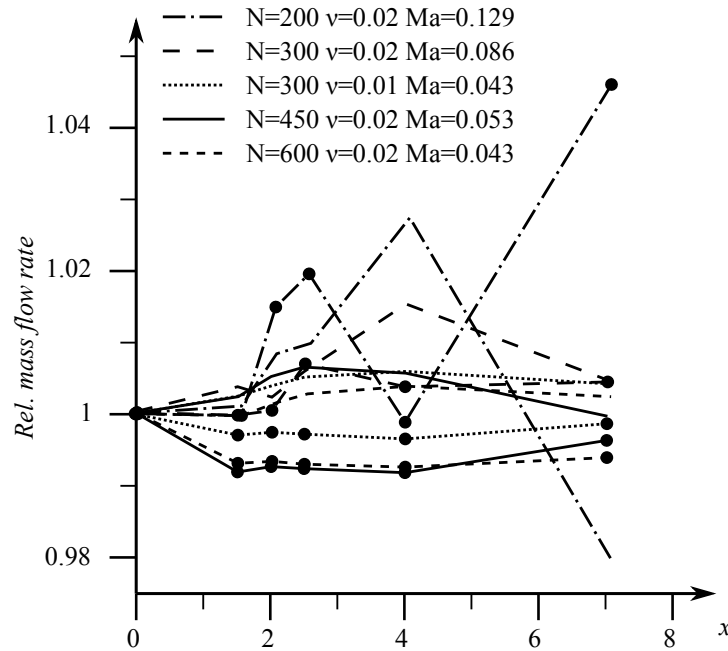


FIG. 13. Relative mass flow rate for different Mach numbers and lattice resolutions in the channel flow. Lines with no marker – phase 0, lines with \bullet – phase 0.25.

was obtained by integrating the horizontal component of the momentum on the consecutive cross-sections of the channel:

$$(3.4) \quad Q = \int_0^1 u_x \rho \, dy \approx \sum_{i=1}^N u_{xi} \rho_i.$$

The variations of mass flow rate along the channel reach 5% in the most compressible case. In this case they oscillate downstream. For less-compressible flows these oscillations do not occur. It should be noted that the Mach number is based on the inlet velocity and locally in the flow it is higher. Thus, the compressibility effect varies in the computational domain. To conclude, the flows with the average Mach number below 0.05 are considered accurate enough and grids of similar size will be used as reference in most cases in the next section. A detailed study of accuracy of the Lattice Boltzmann Method with respect to compressibility effects is available in [25].

4. Flow simulations by means of the Spectral Element Method

4.1. Mathematical formulation

An alternative approach to the Lattice Boltzmann method (LBM) considered in this work is the spectral element method (SEM). As before, the aim is to find the solution of the differential system consisting of the Navier–Stokes equation (1.1) and the continuity equation (1.2), in the flow domain Ω depicted in Fig. 1. The boundary conditions imposed at the inlet and the outlet sections used for the LBM are now replaced by a special variant of the pseudo-traction boundary conditions, usually referred to as the “deficient” or “do-nothing” formulation (see [26], [27]). For the flow considered in this study, these conditions assume the following form:

$$(4.1) \quad p - \nu \frac{\partial}{\partial x} u_x = P(t), \quad \frac{\partial}{\partial x} u_y = 0 \quad \text{at } S_{\text{in}},$$

$$(4.2) \quad p - \nu \frac{\partial}{\partial x} u_x = 0, \quad \frac{\partial}{\partial x} u_y = 0 \quad \text{at } S_{\text{out}}.$$

The function P in (4.1) is not a priori known and it should be determined in such a way that the volumetric flow rate follows a prescribed time variation, meaning that

$$(4.3) \quad \Phi(\mathbf{u}) \equiv \int_{S_{\text{in}}} \mathbf{u} \cdot \mathbf{n} \, ds = - \int_{S_{\text{in}}} u_x \, dy = F(t),$$

where function F is given. Note that neither the velocity profile nor pressure distribution are explicitly determined for the inlet and outlet parts of the boundary $\partial\Omega$.

It can be shown that the function $P(t)$ in the first formula in (4.1) has a straightforward physical interpretation – it describes the time variation of the section-averaged inlet pressure. Similarly, the first of the boundary conditions in (4.2) implies that section-averaged outlet pressure is zero.

To obtain the complete formulation, the initial conditions must be defined, namely

$$(4.4) \quad \mathbf{u}|_{t=t_0} = \mathbf{u}_0.$$

The vector field \mathbf{u}_0 is assumed to satisfy the continuity and volumetric flow rate conditions, i.e., $\nabla \cdot \mathbf{u}_0 = 0$ and $\Phi(\mathbf{u}_0) = F(0)$.

In order to apply the spectral element method, the flow problem should be recast to a weak form, which can be formulated as follows:

Find the velocity vector field $\mathbf{u} \in V = \{\mathbf{v} \in [H_1(\Omega)]^2 : \mathbf{v}|_\Gamma = 0\}$, the pressure field $p \in L^2(\Omega)$ and the function $P = P(t)$ such that

- 1) the equalities

$$(4.5) \quad \begin{cases} (\partial_t \mathbf{u} + \nabla \mathbf{u} \cdot \mathbf{u}, \mathbf{v}) + \nu(\nabla \mathbf{u}, \nabla \mathbf{v}) + P(t)\Phi(\mathbf{v}) - (p, \nabla \cdot \mathbf{v}) = 0, \\ (q, \nabla \cdot \mathbf{u}) = 0, \end{cases}$$

hold for each $\forall \mathbf{v} \in V$ and each $q \in L^2(\Omega)$,

- 2) the condition $\Phi(\mathbf{u}) = F(t)$ holds for each time instant $t \geq 0$,
- 3) the initial condition $\mathbf{u}|_{t=t_0} = \mathbf{u}_0$ is satisfied; the vector field \mathbf{u}_0 fulfills the continuity constrain $\nabla \cdot \mathbf{u}_0 = 0$ and the volumetric flow rate condition at initial time, i.e., $\Phi(\mathbf{u}_0) = F(0)$.

In the equalities (4.5), the bracket symbols $\langle \cdot, \cdot \rangle$ and (\cdot, \cdot) denote the inner products in the $[L^2(\Omega)]^2$ and $L^2(\Omega)$ spaces, respectively. Note also that the function P plays the role of the Lagrange multiplier, which is to be chosen such that the constrain (4.3) is satisfied.

4.2. The solution method

We will briefly summarize the solution method of the flow problem formulated in the previous section. The exposition will be limited to the description of the sequence of numerical problems to be solved during each time step of the flow simulation. We will not discuss details of the spectral element discretization, which is standard, i.e., it uses the quadrilateral elements with the local basic

polynomials based on the Legendre collocation grids. For details of this approach the Reader should refer to the standard monographs like [28], [29] or [30]. We enumerate here the most important features of the in-house solver used in the current study:

1. The second-order Backward Differentiation Formula (BDF) combined with the Operator-Integration-Factor Splitting (OIFS) approach to the nonlinear terms in the Navier–Stokes equations is used [31].
2. The Conjugate Gradients Method (CGM) with an efficient bi-level preconditioning, developed after [32], is applied in the pressure solver. On the level of individual spectral elements, the Fast Diagonalization Method is used.
3. The CGM iterations are initialized with the use of the orthogonal projection method proposed by Fisher [33].

A detailed description of all technical details of the solver as well as relevant implementation issues can be found in the papers [34] and [35].

The key problem, in each time step of the numerical simulation is the determination of such an average inlet pressure $P = P(t)$, where the instantaneous velocity field satisfies the flow rate constrain (4.3). Fortunately, the OIFS approach to convective terms renders the problem linear and the constrain (4.3) can be fulfilled by superposing solutions to appropriately chosen Stokes problems.

The first of these problems can be formulated as follows:

Find the vector field $\mathbf{w} \in V = \{\mathbf{v} \in [H_1(\Omega)]^2 : \mathbf{v}|_T = 0\}$, the scalar field $\zeta \in L^2(\Omega)$ such that the following equalities

$$(4.6) \quad \begin{cases} \frac{\beta_0}{\Delta t} \langle \mathbf{w}, \mathbf{v} \rangle + \nu \langle \nabla \mathbf{w}, \nabla \mathbf{v} \rangle + \Phi(\mathbf{v}) - (\zeta, \nabla \cdot \mathbf{v}) = 0, \\ (\nabla \cdot \mathbf{w}, q) = 0, \end{cases}$$

hold for each $\forall \mathbf{v} \in V$ and each $q \in L^2(\Omega)$.

In the above, the quantity β_0 is the coefficient at the implicit term in the m th-order backward differentiation formula for the first derivative (see [35])

$$(4.7) \quad \partial_t \eta|_{t=t_{n+1}} \approx \sum_{k=0}^{m-1} \beta_k \eta(t_{n+1-k}).$$

For the second-order method used in the current study the coefficients in the formula (4.7) are $\beta_0 = 3/2$, $\beta_1 = -2$ and $\beta_2 = 1/2$.

Note that the solution of the problem (4.6) depends only on the geometry of the domain (we assume that the time step is fixed), thus it can be found once

and forever prior to the main simulation. We will need also the corresponding flow rate

$$(4.8) \quad F_W = \Phi(\mathbf{w}).$$

The computational algorithm for the velocity and pressure fields during each time step can be now explained. Assume that the flow evolution up to the time instant $t = t_n$ is already known and one wants to update the solution to time $t = t_{n+1} = t_n + \Delta t$. The procedure (relevant for the second-order method) consists of the following three steps:

Step 1 (integration of the convective terms accordingly to the OIFS approach)

The following „ordinary” initial value problems (the spatial variables are treated as the parameters)

$$(4.9) \quad \begin{cases} \frac{d}{dt} \hat{\mathbf{u}}_1 = -(\hat{\mathbf{u}}_1 \cdot \nabla) \hat{\mathbf{u}}_1, & t \in [t_n, t_{n+1}], \\ \hat{\mathbf{u}}_1|_{t=t_n} = \mathbf{u}(t_n), \end{cases}$$

$$(4.10) \quad \begin{cases} \frac{d}{dt} \hat{\mathbf{u}}_2 = -(\hat{\mathbf{u}}_2 \cdot \nabla) \hat{\mathbf{u}}_2, & t \in [t_{n-1}, t_{n+1}], \\ \hat{\mathbf{u}}_2|_{t=t_{n-1}} = \mathbf{u}(t_{n-1}), \end{cases}$$

are integrated numerically by the fourth-order Runge–Kutta method using the time step equal $\Delta t_{\text{RK4}} = \Delta t/M$. In the current study, the number of the fine steps performed by RK4 procedure per each major step Δt is $M = 5$. As a result, one obtains the vector fields $\hat{\mathbf{u}}_1(t_{n+1})$ and $\hat{\mathbf{u}}_2(t_{n+1})$.

Step 2 (solution of the main Stokes problem)

The following weakly formulated Stokes problem is solved:

Find the vector field $\mathbf{v} \in V = \{\mathbf{v} \in [H_1(\Omega)]^2 : \mathbf{v}|_\Gamma = 0\}$, the scalar field $\xi \in L^2(\Omega)$ such that the following equalities

$$(4.11) \quad \begin{cases} \frac{3}{2\Delta t} \langle \mathbf{v}, \mathbf{v} \rangle + \nu \langle \nabla \mathbf{v}, \nabla \mathbf{v} \rangle - (\xi, \nabla \cdot \mathbf{v}) \\ \quad \quad \quad = \frac{1}{\Delta t} [2 \langle \hat{\mathbf{u}}_1(t_{n+1}), \mathbf{v} \rangle - \frac{1}{2} \langle \hat{\mathbf{u}}_2(t_{n+1}), \mathbf{v} \rangle], \\ (\nabla \cdot \mathbf{v}, q) = 0, \end{cases}$$

hold for each $\forall \mathbf{v} \in V$ and each $q \in L^2(\Omega)$.

Note that the appropriate linear combination of the auxiliary vector fields $\hat{\mathbf{u}}_1(t_{n+1})$ and $\hat{\mathbf{u}}_2(t_{n+1})$ found in Step 1 appears on the right-hand side of (4.11).

Next, the volumetric flow rate corresponding to the vector field \mathbf{v} is calculated:

$$(4.12) \quad F_V = \Phi(\mathbf{v})$$

Step 3 (updating the section-averaged inlet pressure, construction of the final solution)

The final solution at the time instant $t = t_{n+1} = t_n + \Delta t$ can be written as the superposition of the solutions to the Stokes problems (4.6) and (4.11):

$$(4.13) \quad \mathbf{u}_{n+1} = \mathbf{v} + P_{n+1}\mathbf{w}, \quad p_{n+1} = \xi + P_{n+1}\zeta.$$

The value of the average inlet pressure P_{n+1} at the time instant $t = t_{n+1}$ is such that the volumetric flow rate constrain (4.3) is satisfied. Since

$$(4.14) \quad \Phi(\mathbf{u}_{n+1}) = F_V + P_{n+1}F_W = F(t_{n+1})$$

one immediately gets

$$(4.15) \quad P_{n+1} = [F(t_{n+1}) - F_V]/F_W.$$

It can be easily checked that the updated solution satisfies the following weakly posed problem

$$(4.16) \quad \begin{aligned} \frac{3}{2\Delta t} \langle \mathbf{u}_{n+1}, \mathbf{v} \rangle + \nu \langle \nabla \mathbf{u}_{n+1}, \nabla \mathbf{v} \rangle - (p_{n+1}, \nabla \cdot \mathbf{v}) - P_{n+1} \Phi(\mathbf{v}) \\ = \frac{1}{\Delta t} \left[2 \langle \hat{\mathbf{u}}_1(t_{n+1}), \mathbf{v} \rangle - \frac{1}{2} \langle \hat{\mathbf{u}}_2(t_{n+1}), \mathbf{v} \rangle \right] \end{aligned}$$

which is exactly the second-order BDF/OIFS approximation of the Navier–Stokes equation. Moreover, the velocity field \mathbf{u}_{n+1} satisfies the flow rate condition (4.3) at $t = t_{n+1}$ as required.

5. Comparison of the results of the LBM and the SEM simulations

5.1. Flows past a diamond- and cylinder-shaped obstacles

The aim of the simulations was to cross-validate the Lattice Boltzmann Method versus the Spectral Element Method. Again, the flows at Reynolds numbers of 10, 50, 100 and 200 past a diamond and a cylindrical obstacle were simulated. The flows were compared with respect to the pressure drop and Strouhal number of the vortex street, defined as

$$(5.1) \quad \text{St} = \frac{fD}{U_{\text{bulk}}} = \frac{f_{\text{LB}} N_{\text{obstacle}}}{U_{\text{bulk LB}}},$$

where f and f_{LB} are the frequencies (dimensional and non-dimensional) of the vortex shedding. The obtained results are presented in the Tables 3 and 4. It can be observed that both pressure drops and the dimensionless vortex shedding frequencies (Strouhal numbers) obtained from the LBM and SEM simulations are very much similar – the relative discrepancies remain within the range of several percent. Basically, the flow past a “diamond” obstacle seems to be “more difficult” case and the differences are generally larger (especially in terms of the pressure drop) than in the case of the flow past the circular contour. It is also worth noting that the hydraulic losses computed for diamond obstacle are about 40% larger than for the circular obstacle. This effect has been expected and it can be explained by the fact that the vicinity of the side corners serves as the source of very strong vorticity layers which contribute immensely to the local dissipation of mechanical energy and inflict large pressure drops.

Table 3. Comparison of pressures obtained in LBM and SEM for both types of obstacles. In case of LBM, the pressures are rescaled with $\delta x = 1/300$ cm, $\delta t = 1/45000$ s, $\nu_{LB} = 0.02$, $\nu = 1$ cm²/s², except for diamond at Re = 200, where $\delta x = 1/600$ cm.

	Pressure drop $\frac{\Delta p_{avg}}{\rho} \left[\frac{cm^2}{s^2} \right]$			
	circle		diamond	
Re	LBM	SEM	LBM	SEM
10	0.487	0.492	0.436	0.435
50	3.346	3.310	3.480	3.400
100	8.663	8.603	10.307	10.114
200	25.232	24.620	35.716	35.250

Table 4. Strouhal number of the von Karman vortex street behind the cylinder.

	Strouhal number St			
	circle		diamond	
Re	LBM	SEM	LBM	SEM
100	0.421200	0.420390	0.39120	0.39216
200	0.391500	0.387409	0.37928	0.38095

Additionally to flow resistance and the frequency analysis of the vortex shedding, the comparison of the instantaneous velocity profiles at the Reynolds number Re = 200 has been performed. The velocity profiles were determined for the cross-sections given in Fig. 12. The profiles were computed at four equally spaced time instants within one cycle of the vortex shedding, i.e., every quarter of the time duration of this cycle. The beginning of the probing time has been

set in accordance with the vertical velocity component computed at the control point, as described in Sec. 3. All the LBM simulations except for the flow past the “diamond” at $Re = 200$ were performed on the grid whose dimensions are given in Fig. 14. The flow past a diamond at $Re = 200$ was simulated on the twice denser grid (600×4200 nodes).

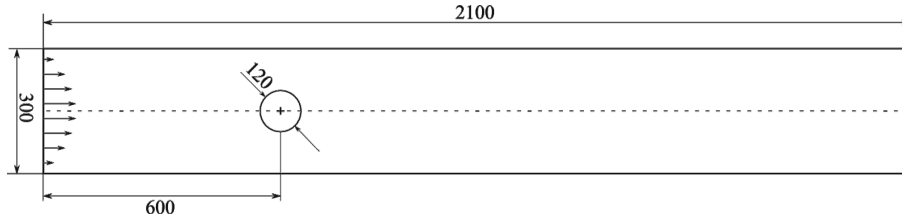


FIG. 14. The shape of the channel with dimensions in lattice units. Either a circle or a diamond are located in the channel. They occupy 40% of the channel’s height.

In case of the LBM, the parabolic profile of the inlet velocity has been enforced explicitly by the boundary condition. In case of the SEM, the velocity profile evolves by itself towards the parabolic shape as the result of the “do-nothing” boundary conditions with imposed volumetric flow. It is worth noting that the vertical component of inlet velocity in the SEM computations is not exactly zero but it is smaller by several orders of magnitude than the stream-wise component. Thus, one can conclude that the upstream influence of the obstacle’s presence on the flow structure at this distance is negligible (see Figs. 15 and 16).

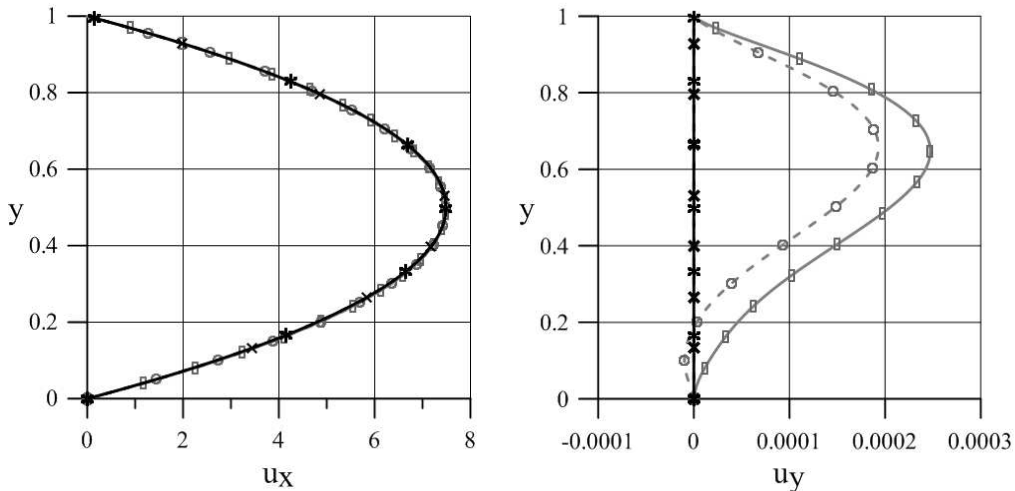


FIG. 15. The profiles of x (left) and y (right) inlet (cross-section P_1) velocity components in the flow past a diamond obstacle. The following legend is valid for the Figs. 15–26: * – LBM, $T = 0$, \times – LBM, $T = 0.25$, \square SEM, $T = 0$; \bullet – SEM, $T = 0.25$.

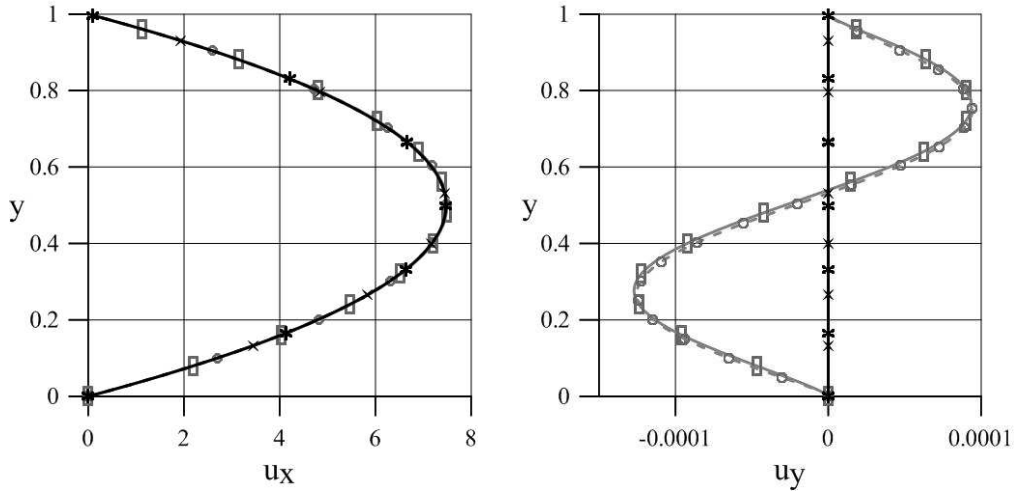


FIG. 16. The profiles of x (left) and y (right) inlet (cross-section P_1) velocity components in the flow past the circular obstacle.

Coming closer to the obstacle, the deviations from parabolic profile becomes more noticeable and the vertical component of the velocity grows. The agreement between instantaneous velocity profiles obtained by both methods in consecutive cross-sections of the channel is really good (cross-section P_2 , Fig. 17, 18).

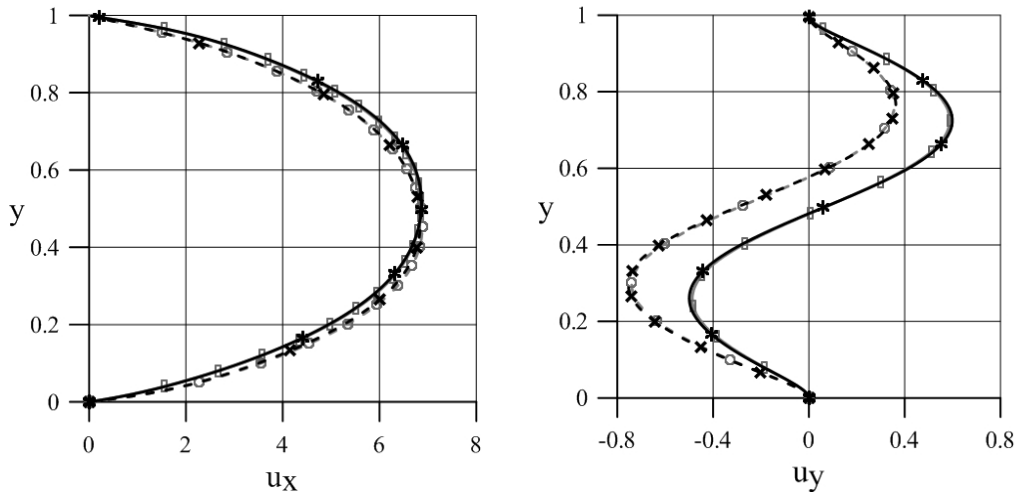


FIG. 17. The profiles of x (left) and y (right) velocity components in the flow past a diamond obstacle, computed in the channel's section P_2 .

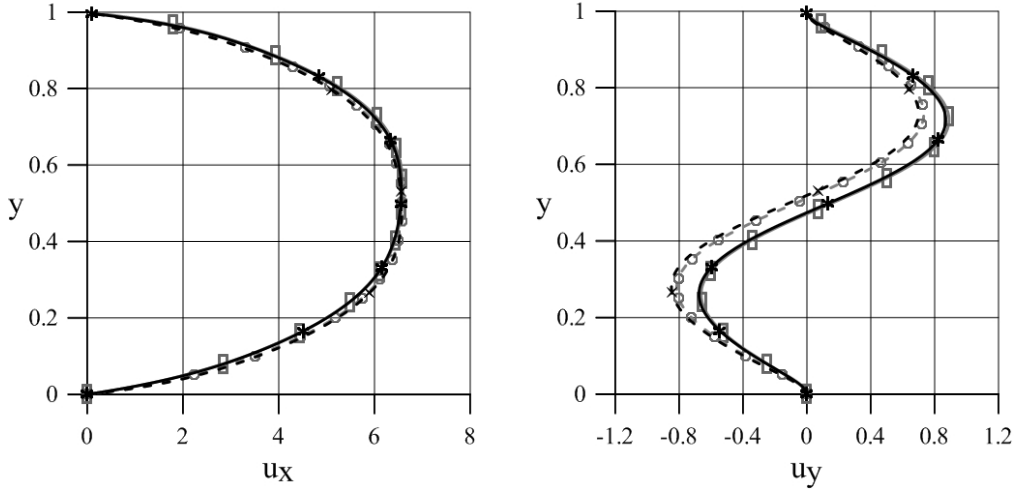


FIG. 18. The profiles of x (left) and y (right) velocity components in the flow past a circular obstacle, computed in the channel's section P_2 .

Just at the obstacle (cross-section P_3 , Figs. 19, 20) one can observe a huge vertical gradient of the vertical velocity component. It is steeper in case of “diamond” due to the fact that geometry is not smooth. In case of circle, one can notice a very good symmetry of the horizontal velocity component. It is not the

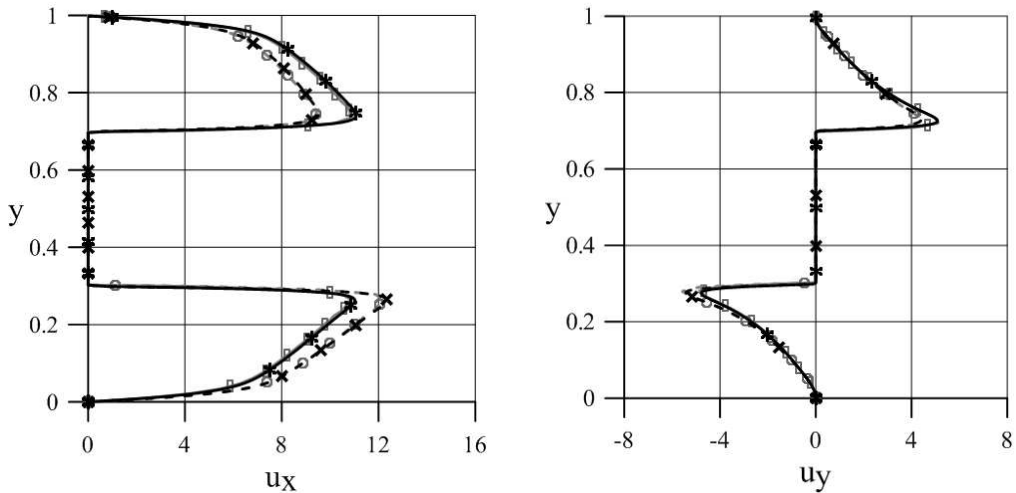


FIG. 19. The profiles of x (left) and y (right) velocity components in the flow past a diamond obstacle, computed in the channel's section P_3 . Note that in the range of y between 0.3 and 0.7 the section P_3 penetrates the obstacle.

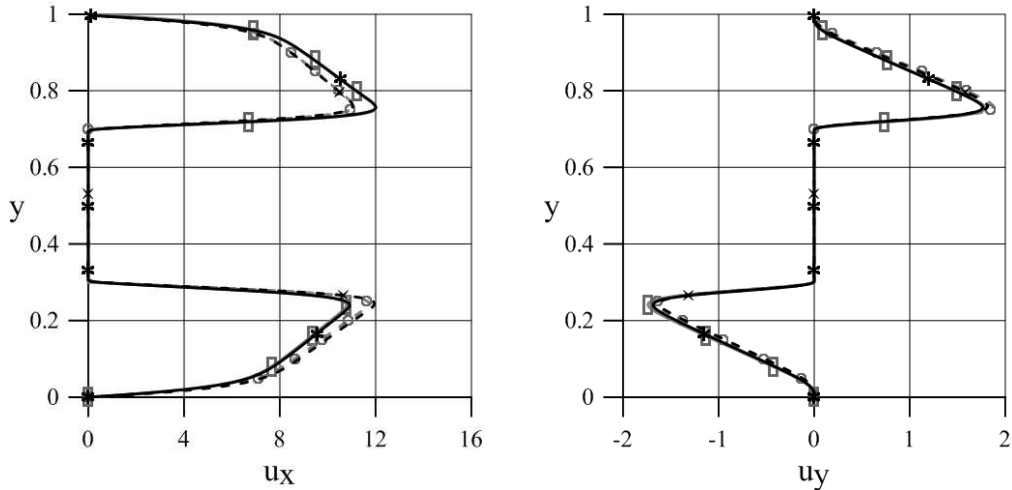


FIG. 20. The profiles of x (left) and y (right) velocity components in the flow past a circular obstacle, computed in the channel's section P_3 . Note that in the range of y between 0.3 and 0.7 the section P_3 penetrates the obstacle.

case of the flow past the “diamond”. The LBM and SEM still, however, give very similar results.

In the wake behind the cylinder, one can observe the vortex street. Its presence in the velocity profiles is marked by large variations of the vertical velocity component (Figs. 21, 22). The results from both methods start to exhibit slight differences.

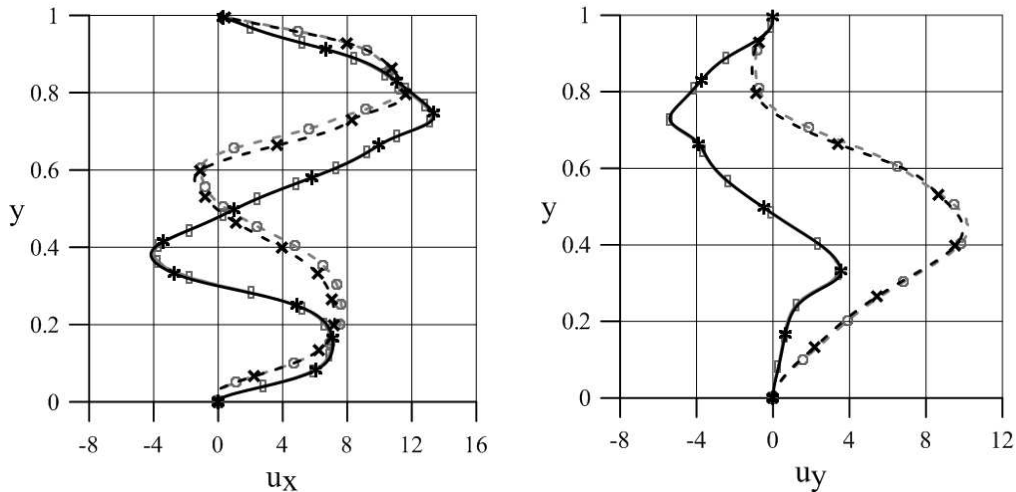


FIG. 21. The profiles of x (left) and y (right) velocity components in the flow past a diamond obstacle, computed in the channel's section P_4 .

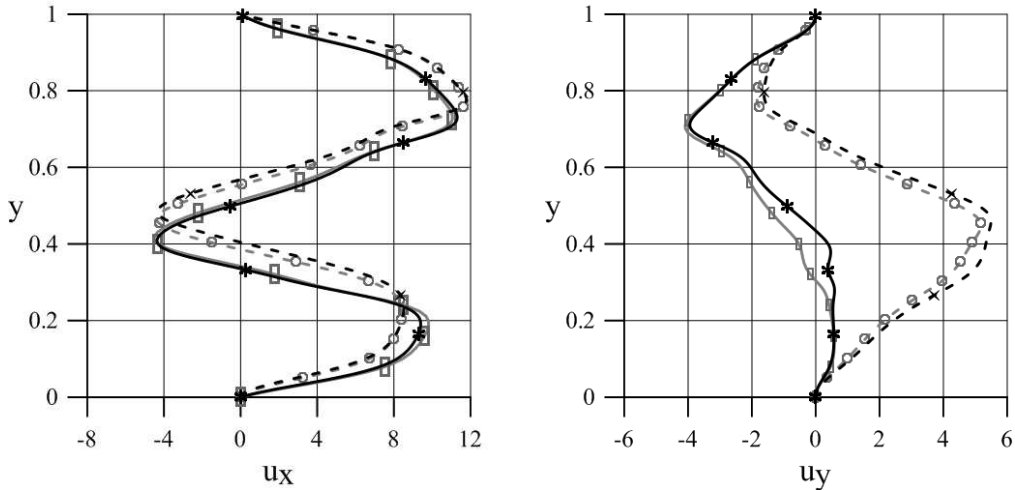


FIG. 22. The profiles of x (left) and y (right) velocity components in the flow past a circular obstacle, computed in the channel's section P_4 .

Further downstream one continues to observe the vortices (Figs. 23, 24). From the magnitude of the vertical velocity one can state that the intensity of the vortex street shed from the diamond obstacle is much stronger. The agreement between the LBM and SEM is much worse in the case of vertical velocity for circular cylinder (Fig. 24). Better accuracy for the “diamond” should be attributed to higher resolution of the case.

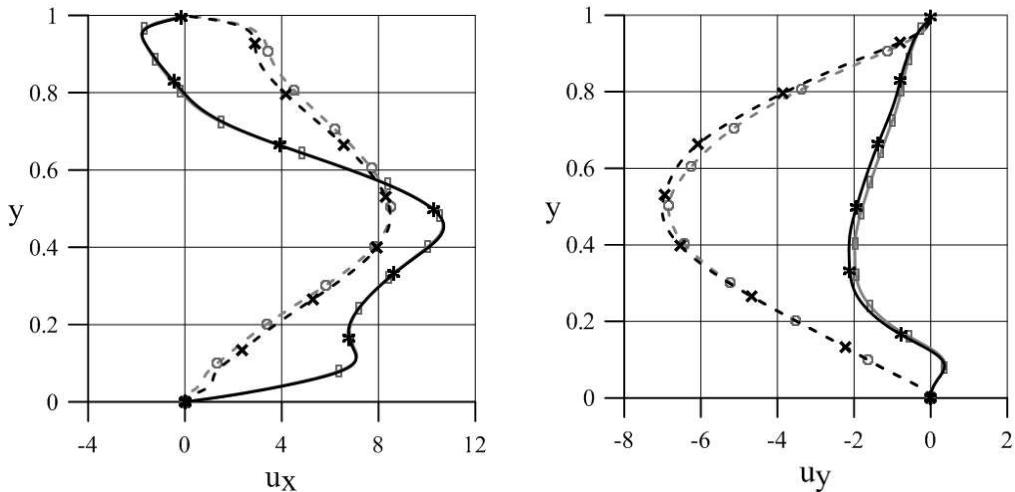


FIG. 23. The profiles of x (left) and y (right) velocity components in the flow past a diamond obstacle, computed in the channel's section P_5 .

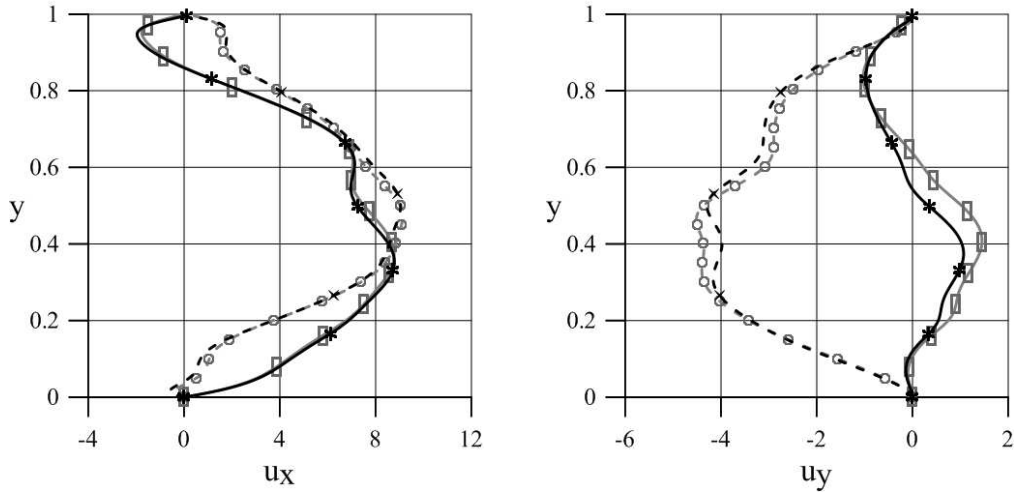


FIG. 24. The profiles of x (left) and y (right) velocity components in the flow past a circular obstacle, computed in the channel's section P_5 .

At the outlet of the channel the vertical component of velocity is set to zero in case of the LBM due to the construction of the outlet boundary condition. The horizontal components of velocity, however, are still in almost perfect agreement for the diamond (Fig. 25) and only slightly deviate from one another in the case of the circular obstacle (Fig. 26).

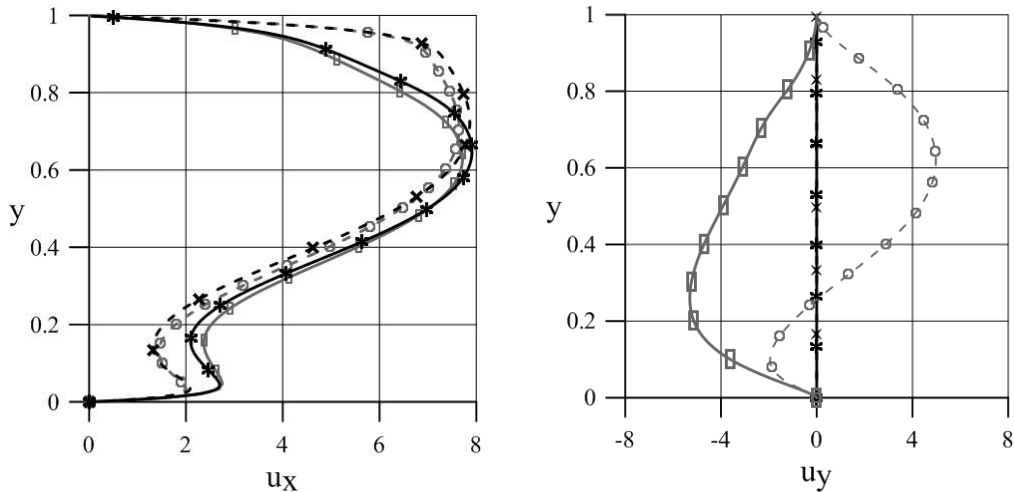


FIG. 25. The profiles of x (left) and y (right) velocity components in the flow past a diamond obstacle, computed in the channel's outlet section P_6 .

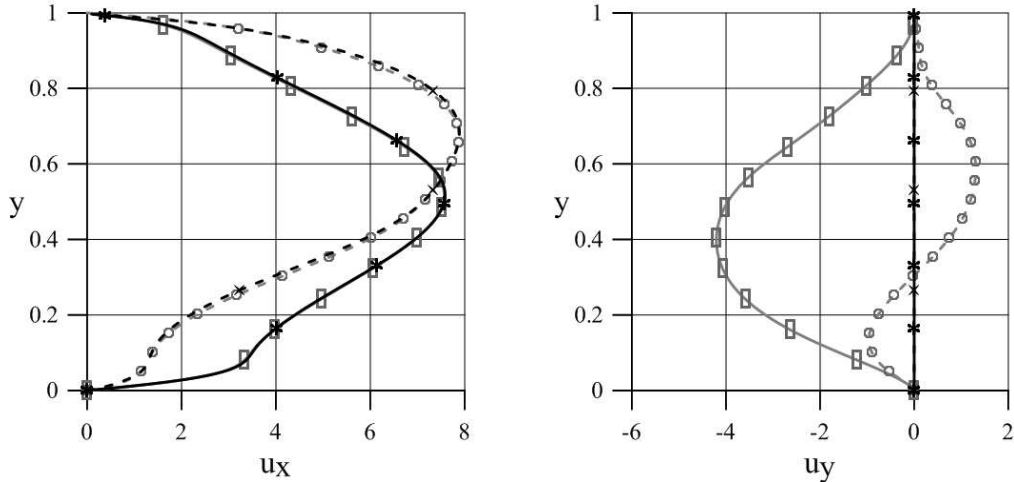


FIG. 26. The profiles of x (left) and y (right) velocity components in the flow past a circular obstacle, computed in the channel's outlet section P_6 .

To sum up, both test cases prove a really good capability of the Lattice Boltzmann Method to reproduce the complex phenomena in unsteady laminar regime of the flow. The instantaneous flow structures computed using the LBM and SEM techniques are in very good agreement, especially in the vicinity of the obstacle and in the close wake. Some differences observed further downstream appear mostly due to the difference in the formulation of the outlet boundary conditions in both methods. As one should expect, a better resolution in case of the diamond shaped obstacle results in a better accuracy of the simulation.

In the end of this section, we present the instantaneous patterns of the wall-confined flow past the “diamond” obstacle. The form contour maps of the velocity magnitude and instantaneous streamlines, computed for two time instants separated by the quarter of the time period of the vortex shedding are presented in Fig. 27. Except the large separation zones and related vortices just behind the obstacle, the big separation bubbles induced by the vorticity shed from the obstacle and rolling along both walls can be seen. This type of flow pattern is very characteristic for the confined flow with moderate blockage ratios.

In Figure 28, the corresponding pressure field is depicted. One can easily notice the street of local minima of pressure that correspond to instantaneous positions of shed vortices. These locations match very well with the regions of large positive and negative vorticity seen in the contour map presented in Fig. 29. Yet another characteristic feature of the wall-confined flows past obstacles is also

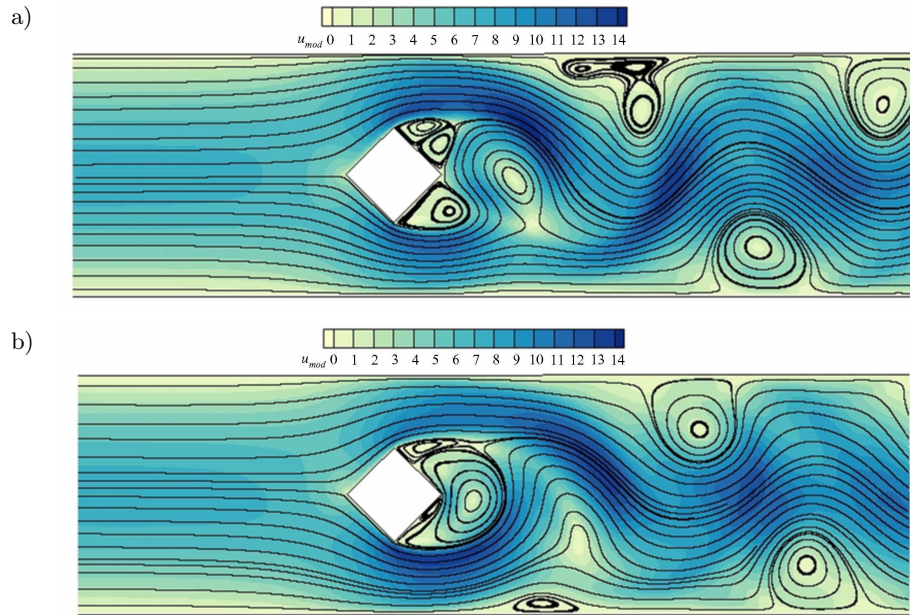


FIG. 27. The contour maps of the magnitude of instantaneous velocity field and the corresponding streamlines pattern, computed for: a) at time instant when the y -component of the velocity field at the control point in the wake behind the obstacle changes sign from negative to positive, b) at the time instant later by a quarter of the vortex shedding period. Flow field obtained with SEM.

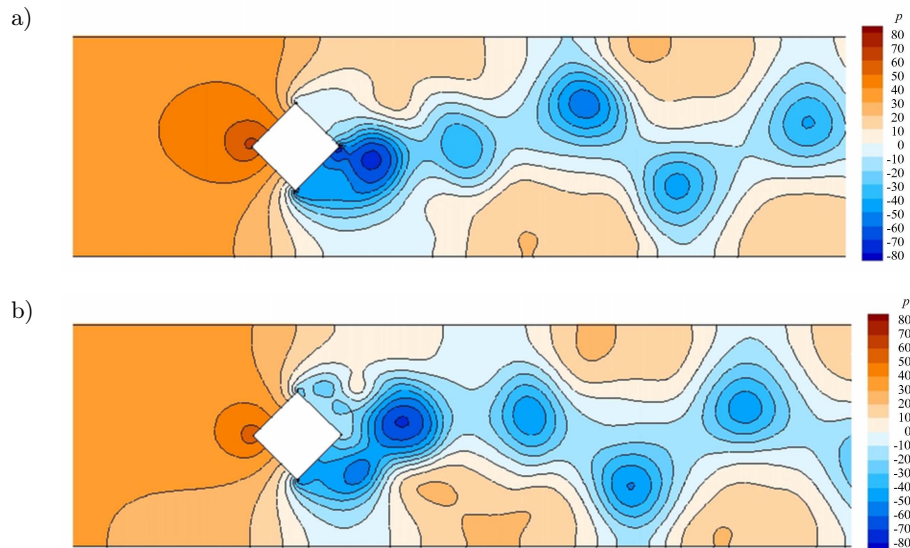


FIG. 28. The instantaneous patterns of the pressure field of the confined flow past the diamond obstacle. The time instants have been chosen in the same way as for the velocity field presented in Fig. 27. Flow field obtained with SEM.

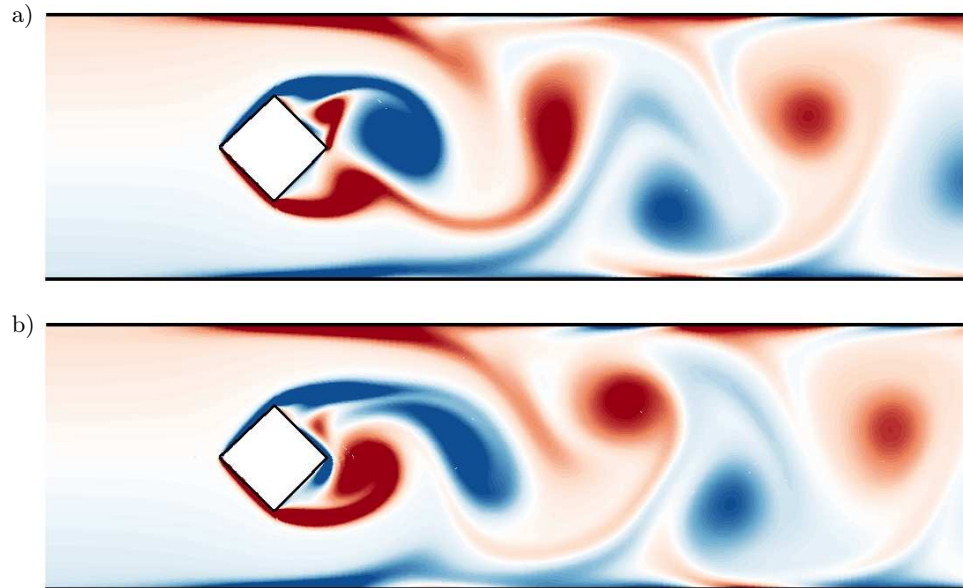


FIG. 29. The instantaneous patterns of the vorticity field of the confined flow past the diamond obstacle. The time instants have been chosen in the same way as for the velocity field presented in Fig. 27. Shades of red and blue colors correspond, respectively, to positive and negative vorticity. Flow field obtained with SEM.

evident: the von Karman vortex street is actually reversed, i.e., the vortices shed from the obstacle's lower side corner are advected towards the top wall and vice versa.

6. Summary and conclusions

The Lattice Boltzmann Method with detailed description of the BGK collision model has been presented and its capabilities to simulate laminar flow of a Newtonian fluid have been verified on the test case of flow in a two-dimensional channel. The influence of compressibility and stair-case representation of geometry on the flow quality has been investigated. Furthermore, the simulations with the LBM have been validated with use of the Spectral Element Method: the flow characteristics such as Strouhal number have been compared and very good agreement between the two methods has been observed. Additionally, instantaneous velocity profiles at various cross-sections of the channel have been compared. Again, the results obtained in both simulation techniques match very well – both in terms of the flow physics and quantitative characteristics – even though the inlet/outlet condition used within the LBM and SEM computations were different. It should be noted that the current version

of the PALABOS package does not incorporate the “do-nothing” variant of the inlet/outlet conditions. On the other hand, further progress in this respect can be expected as the formulation of such conditions for the LBM has recently been proposed [36].

Acknowledgments

The work has been supported by the Polish Ministry of Science and Higher Education and the National Science Centre, research grant no N N507 273636.

References

1. U. FRISCH, B. HASSLACHER, Y. POMEAU, *Lattice gas automata for the Navier–Stokes equations*, Phys. Rev. Lett., **56**, 1505, 1986.
2. S. SUCCI, P. SANTANGELO, R. BENZI, *High resolution lattice gas simulation of two-dimensional lattice gas turbulence*, Phys. Rev. Letters, **60**, 2738, 1988.
3. S. CHEN, H. CHEN, D. MARTINEZ, W. MATTHAEUS, *Lattice Boltzmann model for simulation of magnetohydrodynamics*, Phys. Rev. Lett. **67**, 27, 3776, 1991.
4. N.S. MARTYS, H. CHEN, *Simulation of multicomponent fluids in complex three-dimensional geometries by the lattice Boltzmann method*, Phys. Rev. E, **53**, 743–750, 1996.
5. N.S. MARTYS, F.F. DOUGLAS, *Critical properties and phase separation in lattice Boltzmann mixtures*, Phys. Rev. E, **63**, 1–18, 1991.
6. D. D’HUMIÈRES, A. CLOQUEUR, P. LELLAMAND, *Lattice gas and parallel processors*, Il Calcolo, **25**, 129, 1987.
7. J. F. HIGUERA, S. SUCCI, *Simulating the flow around a circular cylinder with a lattice Boltzmann equation*, Europhys. Lett., **8**, 517, 1989.
8. J. BERNSDORF, T. ZEISER, G. BRENNER, F. DURST, *Simulation of a 2D channel flow around a square obstacle with lattice-Boltzmann (BGK) automata*, International Journal of Modern Physics C, **9**, No. 8, 1129–1141, 1998.
9. M. BREUER, J. BERNSDORF, T. ZEISER, F. DURST, *Accurate computations of the laminar flow past a square cylinder based on two different methods: lattice-Boltzmann and finite-volume*, International Journal of Heat and Fluid Flow, **21**, 2, 186–196, 2000.
10. P.P. PATIL, S. TIWARI, *Effect of blockage ratio on wake transition for flow past square cylinder*, Fluid Dynamics Research, **40**, 753–778, 2008.
11. A. SOHANKAR, C. NORBERG, L. DAVIDSON, *Numerical simulation of unsteady low-Reynolds number flow around rectangular cylinders at incidence*, Journal of Wind Engineering and Industrial Aerodynamics, 189–201, 1997.
12. A. PRZĄDKA, J. SZUMBARSKI, *Numerical analysis of the wake structure in the two-dimensional wall-confined flow past a square cylinder*, 19th Polish National Fluid Dynamics Conference, Poznań, September 5–9, 2010.

13. U. FRISCH, D. D'HUMIERES, B. HASSLACHER, P. LALLEMAND, Y. POMEAU, J.P. RIVET, *Lattice gas hydrodynamics in two and three dimensions*, Complex Systems, **1**, 649, 1987.
14. P. LALLEMAND, L. LUO, *Theory of the lattice Boltzmann method: Dispersion, dissipation, isotropy, Galilean invariance, and stability*, Phys. Rev. E, 6546–6562, 2000.
15. Q. ZOU, X. HE, *On pressure and velocity flow boundary conditions and bounceback for the lattice Boltzmann BGK model*, Phys. Fluids, **9**, 1591–1598, 1997.
16. P. BHATNAGAR, E.P. GROSS, M. KROOK, *A model for collisional processes in gases I: Small amplitude process in charged and neutral one-component system*, Phys. Rev., **94**, 511–525, 1954.
17. D. D'HUMIERES, I. GINZBURG, M. KRAFCZYK, P. LALLEMAND, L. LUO, *Multiple-relaxation-time lattice Boltzmann models in three dimensions*, Phil. Trans. Royal Society London A, 437–452, 2002.
18. P.A. SKORODOS, *Initial and boundary conditions for the lattice Boltzmann method*, Phys. Rev. E, **48**, 4823, 1993.
19. T. INAMURO, M. YOSHINO, F. OGINO, *A non-slip boundary condition for lattice Boltzmann simulations*, Phys. Fluids, **7**, 2928, 1996.
20. R.S. MEIER, R.S. BERNARD, D.W. GRUNAU, *Boundary conditions for the lattice Boltzmann method*, Phys. Fluids, **8**, 1788, 1996.
21. S. SUCCI, *The Lattice Boltzmann Equation for Fluid Dynamics and Beyond*, Oxford University Press, 2001.
22. <http://www.palabos.org/>.
23. R. MEI, W. SHYY, L.-S. LUO, *An accurate curved boundary treatment in the Lattice Boltzmann Method*, Journal of Computational Physics, **155**, 307–329, 1999.
24. J. BAO, P. YUAN, L. SCHAEFER, *A mass conserving boundary condition for the lattice Boltzmann equation method*, Journal of Computational Physics, **227**, 8472–8487, 2008.
25. R.S. MAIER, R.S. BERNARD, ACCURACY OF THE LATTICE-BOLTZMANN METHOD, [in:] Proceedings of the Sixth International Conference on Discrete Models for Fluid Mechanics. Boston University, Boston, 26–28 August 1996. Int. Journal Modern Physics C, **8**, 4, 747–752, 1997.
26. J.G. HEYWOOD, R. RANACHER, S. TUREK, *Artificial boundaries and flux and pressure conditions for the incompressible Navier–Stokes equations*, Int. J. Numerical Methods in Fluids, **22**, 325–352, 1996.
27. L. FORMAGGIA, J.F. GERBEAU, F. NOBILE, A. QUARTERONI, *Numerical treatment of defective boundary conditions for the Navier–Stokes equations*, SIAM Journal of Numerical Analysis, **40**, no. 1, 373–401, 2002.
28. M.O. DEVILLE, P.F. FISHER, E.H. MUND, *High-Order Methods for Incompressible Fluid Flow*, Cambridge University Press, 2002.
29. G.M. KARNIADAKIS, S. SHERWIN, *Spectral/hp Element Methods for Computational Fluid Dynamics*, Oxford Science Publications, 2005.
30. C. CANUTO, M.Y. HUSSAINI, A. QUARTERONI, T.A. ZANG, *Spectral Methods: Evolution to Complex Geometries and Application to Fluid Dynamics*, Springer, 2007.

31. Y. MADAY, A.T. PATERA, E.M. RONQUIST, *An operator-integration-factor splitting method for time-dependent problems: Application to incompressible fluid flow*, J. Sci. Comput., **5**, 263–292, 1990.
32. W. COUZY, M.O. DEVILLE, *Spectral-element preconditioners for the Uzawa pressure operator applied to incompressible flows*, J. Scientific Computing, **9**, 2, 107–122, 1994.
33. P.F. FISHER, *Projection techniques for iterative solution of $Ax = b$ with successive right-hand sides*, Comput. Methods. Appl. Mech. Eng., **163**, 193–204, 1998.
34. J. SZUMBARSKI, P. OLSZEWSKI, A. STYCZEK, J. ROKICKI, *Computations of an unsteady flow in a three dimensional system of ducts. Part 1: Formulation of the mathematical problem and numerical method*, Journal of Theoretical and Applied Mechanics, **42**, 1, 21–39, 2004.
35. J. SZUMBARSKI, P. OLSZEWSKI, K. WAWRUCH, Z. MAŁOTA, *Computations of an unsteady flow in a three dimensional system of ducts. Part 2: Implementation issues and sample results*, Journal of Theoretical and Applied Mechanics, **42**, 4, 869–903, 2004.
36. M. JUNK, Z. YANG, *Pressure boundary condition for the lattice Boltzmann method*, Computers and Mathematics with Applications, **58**, 922–929, 2009.

Received November 29, 2011; revised version March 22, 2012.
